Tracking CO_2 plumes in clay-rich rock by distributed fiber optic strain sensing (DFOSS): a laboratory demonstration

Yi Zhang[1,2*], Ziqiu Xue[1,2], Hyuck Park[1,2], Ji-Quan Shi[3], Tamotsu Kiyama[1,2], Xinglin Lei[4], Yankun Sun[1,2],Yunfeng Liang[5]

[1]Geological Carbon dioxide Storage Technology Research Association, 9-2, Kizugawadai, Kizugawa Shi, Kyoto, 6190292 Japan

[2]Research Institute of Innovative Technology for the Earth (RITE), 9-2, Kizugawadai, Kizugawa-Shi, Kyoto, 619-0292 Japan.

[3]Department of Earth Science and Engineering, Royal School of Mines, Imperial College London, London SW7 2BP, United Kingdom.

[4]Geological Survey of Japan, National Institute of Advanced Industrial Science and Technology, AIST Central #7, Higashi 1-1-1, Tsukuba, Ibaraki 305-8567, Japan.

[5]Center for Engineering, Research into Artifacts (RACE), The University of Tokyo, Kashiwa, Chiba 277-8568, Japan.

Corresponding author: Yi Zhang (zhangyi@rite.or.jp)

Key Points:

- Rock deformation during supercritical CO_2 /brine displacement was measured using an advanced high-resolution DFOSS tool.
- The adsorption-induced swelling in clay-rich rocks can serve as a "saturation footprint" for tracking CO_2 migration in reservoirs.
- The breakthrough of CO_2 plume from the high-permeability to low-permeability part was well captured using the distributed strain.

Abstract

Monitoring the migration of pore pressure, deformation, and saturation plumes with effective tools is important for the storage and utilization of fluids in underground reservoirs, such as geological stores of carbon dioxide (CO_2) and natural gas. Such tools would also verify the security of the fluid contained reservoir–caprock system. Utilizing the swelling strain attributed to pressure build-up and the adsorption of supercritical CO_2 on clay minerals, we tracked the fluid plume in a natural clay-rich Tako sandstone at the laboratory core-scale. The strain was measured by a high-resolution distributed fiber optic strain sensing (DFOSS) tool. The strain changes induced by CO_2 adsorptions on clay minerals were significantly greater than those caused by pore pressure alone. The distribution of the swelling-strain signals effectively captured the dynamic breakthrough of the CO_2 plume from the high- to low- permeability regions in the Tako sandstone. Besides revealing the in situ deformation state, the measured strain changes can track the movement of the CO_2 plume as it enters the clay-rich critical regions in the reservoir–caprock system. The present findings and potential future applications of DFOSS in the field are expected to enhance the monitoring and management of underground fluid reservoirs.

Plain Language Summary

Carbon dioxide (CO_2) sequestration in underground geological reservoirs is considered as a near-term solution to global warming. However, monitoring the migration of sequestered CO_2 in deep reservoirs is inherently difficult. Here, the well-known adsorption-induced swelling phenomenon in clay-rich rocks is considered as a naturally generated "saturation footprint" that tracks CO_2 migration through reservoirs. When a CO_2 plume migrates in a storage reservoir–caprock system, the CO_2 can be adsorbed on/in the clay-rich components, leaving footprints of rock swelling. By tracking these footprints, we expect to monitor the migration of CO_2 plumes. To test this idea at the laboratory scale, we measured the strain changes during dynamic CO_2/brine displacements in a clay-rich rock using a high-resolution Rayleigh-scattering based distributed fiber optic strain sensing (DFOSS) tool. The fluid distribution in the rock was then determined by X-ray computed tomography imaging. Large swelling strains and shrinkage strains were observed during CO_2 drainage and brine re-imbibition, respectively. Moreover, the distributed strain signals clearly revealed the breakthrough of the CO_2 plume from the high- to low- permeability regions. The results suggest that the strain change, measured by the powerful DFOSS tool, not only reveals the in-situ deformation state but also tracks the movement of the CO_2 plume as it enters the clay-rich critical regions in a reservoir–caprock system.

1 Introduction

Underground geological reservoir engineering, such as enhanced oil recovery by water or gas injection, geothermal exploitation, shale gas fracking, and natural gas and CO_2 storage, often involves fluid injections and/or extractions. These operations inevitably change the in situ pressure state in the porous space, leading to mechanical deformations in the geological formations. Deformations arise by the poroelastic mechanism, which describes the coupling between pore fluid-flow and porous-matrix deformations under stress. The deformations may be sufficient to induce seismicity (Gan & Frohlich, 2013; Hincks et al., 2018; Zoback & Gorelick, 2012), or observable uplift or subsidence of the ground (Rutqvist, 2012; Shirzaei et al., 2016).

CO_2 sequestration into underground geological reservoirs is considered as a near-term solution to global warming effects (Benson et al., 2005; Celia, 2017; Sanchez et al., 2018). CO_2 injected into rocks can be retained by capillary, solubility, structure, and mineral trapping mechanisms. In large-scale geological CO_2 storage projects, pressure build-up affects the long-term integrity of the CO_2 repository, increasing the risk of CO_2 or brine leakages. If the pressure in the reservoir overwhelms the threshold pressure of caprock, the CO_2 will migrate into the caprock. In addition, fault reactivations and caprock breaches can create or enhance vertical leakage pathways that unexpectedly leak CO_2 (White et al., 2014; Zoback & Gorelick, 2012). For these reasons, the spatial development of pressure build-up, deformation, and CO_2 plume migration in the reservoir formations and caprocks above the storage reservoir, must be monitored by reliable methods (Verdon et al., 2013).

The distributed fiber optic strain sensing (DFOSS) technique, which has been recently developed, tracks the response to rock deformation at each spatial location along a fiber-installed crossing-formation wellbore in real-time (Kogure & Okuda, 2018; Wu et al., 2017; Xue & Hashimoto, 2017). Therefore, this technique can potentially improve our understanding of pressure and CO_2 plume migrations along the vertical direction while performing in-reservoir and above-zone pressure monitoring (Strandli & Benson, 2013). An example is the Decatur CO_2 storage site in Illinois, USA (Cameron et al., 2016). The technique also gives important constraints for geomechanical modeling and enables surface deformation monitoring (Maharramov & Zoback, 2018; Rutqvist & Tsang, 2002; Shi et al., 2012; Vasco et al., 2010).

Besides poroelastic deformation, clay swelling phenomena (which are a poromechanical response) have been extensively studied in shales, coals, soils, and other geophysical fields. When CO_2 is energetically adsorbed on the surfaces and edges of clay minerals, or incorporated into crystal interlayers (Wan et al., 2018), significant swelling occurs (Busch et al., 2016; Romanov & Myshakin, 2018). The swelling can be sufficiently large to change the stress state (Wentinck & Busch, 2017). At any given pressure, carbon dioxide causes more pronounced swelling than other fluids, such as water and methane (Heller & Zoback, 2014). Therefore, as CO_2 displaces brine from clay-rich strata (e.g., caprocks), it should be possible to measure the strain changes due to the preferential adsorption of CO_2 in the clay, in addition to the poroelastic mechanism. Considering this mechanism, we monitored the migration of the CO_2/brine displacement front in clay-rich regions in a reservoir–caprock system by measuring the strain using the DFOSS technique (Figure 1a). The study sample was a clay-rich Tako sandstone from Gunma, Japan, which has developed both high-permeability and low-permeability regions (Figure 1b). The strain in the sample was continuously measured during CO_2 drainage and brine imbibition under typical reservoir conditions (10 MPa and 40 °C), and the fluid saturation was imaged by X-ray computed tomography (CT).

2 Experimental materials and methods

The rock sample was cored through a low-permeability (0.02 mD) Tako sandstone (Gunma, Japan), along the direction perpendicular to the bedding plane. The sample was cylindrical with a diameter and length of 35 mm and 80 mm respectively. It was visually divided into two regions (coarse-grained and fine-grained; see Figure 1b) with different petrophysical characteristics. Specifically, the permeability, porosity (Figure S1) and pore size (Figure S2) were larger in the coarse-grained part than in the fine-grained part. Both parts were rich in the clay mineral kaolinite (Figure S3). In an X-ray powder diffraction (XRD) analysis, the mineral compositions of the two parts (coarse and fine) were determined as follows: quartz (52.2% and 38.0%), kaolinite (36.0% and 52.8%), muscovite (2.8% and 8.3%), and K-feldspar (8.0% and 0.9%) (Figure S4). The sample was a mini analog of an actual reservoir–caprock system, exhibiting the typical transition from caprock to reservoir, sand–mud alternation, tight interbedding layers within the reservoir, and faults with clay smearing (Figure 1a). The rocks in these components are usually clay-rich and less permeable than common reservoir sandstones.

For strain measurements, a single-mode holey optical fiber fabricated from silica (Hitachi Cable Ltd.) was spirally bonded to the surface of the cylindrical sample (Figure S5). The fiber strain (ε_{f}) along the spiral path is related to the circumferential strain in the rock (ε_{c}) as follows (Li, 2016; Rambow et al., 2010):

$$\varepsilon_{\mathrm{f}} = \sqrt{\sin^2(\theta)(1-\nu\varepsilon_{\mathrm{c}})^2) + \cos^2(\theta)(1+\varepsilon_{\mathrm{c}})^2)}, \quad (1)$$

where ν is the Poisson's ratio of the rock and θ is the wrapping angle. Under the conditions of the present study (θ ~ 5° **(**Figure S5**)**, $\nu = 0.31$, $\varepsilon_{\mathrm{f}} = 0.99\varepsilon_{\mathrm{c}}$), the DFOSS technique mainly measured the circumferential component of the rock deformation. Because the cladding surrounding the glass core of the fiber was punctuated with holes, the bending loss of the light signals was low, allowing measurements under considerable surface bending (the minimum allowed bending radius was 5 mm). When wrapping around the rock surface, the fiber was pre-strained by hitching under a weight of approximately 300 g. The pre-strain prevented the fiber from breaking or slipping from the cementing paste during the contractive deformation. The fiber was directly contacted with the rock surface and fixed by an epoxy adhesive coating (High Super 5, Cemedine Co., Ltd.).

To insulate the confining oil and pore fluids under the high injection pressure and confining pressure, the sample was then jacketed in another epoxy adhesive (EP001K, Cemedine Co., Ltd.) and placed in a core holder (Figure S6) made of an X-ray transparent and high-strength material (PEEK). The pressure and fluid injections were controlled by two accurately dispensing syringe pumps, each connected to one side of the rock sample. The CO_2 was maintained in a supercritical condition under a pore pressure above 10 MPa and a temperature of 40 °C. Here, the temperature of the whole system was maintained by carbon cloth heaters or water circulation heaters. The fiber was passed through the pressurized core holder by a feedthrough component, which prevented the leakage of fluids. The entire core holder was placed on the bed of a medical X-ray CT scanner for imaging. The fiber segments outside the core holder were connected to two prolonged segments of single-mode optical fiber cable with a thicker sheath and then connected to an interrogator (Neubrex 7020 type, Neubrex Co., Ltd., Kobe, Japan). Both types of optical fibers were spliced by a fiber fusion splicer (FSM-60S, Fujikura Ltd., Tokyo, Japan).

The DFOSS tool uses the coherent optical time-domain reflectometer (COTDR) method (Kishida et al., 2014), which calculates the strain or temperature from the shifted power frequency spectra of the Rayleigh backscatter traces (Koyamada et al., 2009). The Rayleigh backscattering signals are produced from inherent random defects or heterogeneities in the fiber core (Kishida et al., 2014; Koyamada et al., 2009). The light source of the COTDR is precisely frequency-controlled. The frequency shift between the measurements before and after the environmental change is calculated by cross-correlation. If the strain or temperature at a spatial location of the fiber is unchanged during the specified time interval, the two power spectra will coincide in the frequency domain. On the contrary, a strain or temperature change will alter the local refractive index, inducing a phase shift between the power spectra. The changes in temperature or strain are linearly related to the frequency shifts (Kishida et al., 2014):

$$\Delta f_{\mathrm{R}} = a\Delta\epsilon + b\Delta T, \quad (2)$$

where Δf_{R} is the overall frequency shift, $\Delta\epsilon$ and ΔT are the strain and temperature changes, respectively, and a and b are the calculation coefficients for the strain and temperature, respectively. In this study, the temperature remained constant throughout the test, so the frequency shifts in the Rayleigh backscattering were wholly attributable to the strain changes. In preliminary laboratory tests of the optical fiber, a was determined as -0.153 GHz/με. To include the strain transfer effects, the coefficient was measured without removing the surface coating material (UV-curable acrylate resin) from the cable, and after bonding with the epoxy adhesive. These fiber conditions matched those of the strain measurements during the core-flooding test.

The DFOSS tool can monitor small strains at high measurement accuracy (0.5 με) and spatial resolution (2 cm) over a long-range distribution (~ 25 km). The accuracy of the DFOSS technique has been demonstrated in several prior comparison tests with conventional strain gauges (Kogure et al., 2015; Xue et al., 2014). The technique has also been successfully applied in water injection tests and measurements of field wellbores (Xue & Hashimoto, 2017). Note that previously fiber Bragg grating strain sensor has been applied to detect the fluid front (Sun et al., 2017). The present study demonstrates the improved performance of monitoring with the high-resolution, distribution-focused DFOSS tool.

To understand the fluid flow behavior, the fluid saturation in the rock sample during the fluid displacements was imaged by a medical X-ray CT scanner (Aquilion ONE TSX 301A). The image volume of each CT scan was constructed from 160 slices along the axial direction (of length 80 mm). Each slice was composed of 512×512 pixels, each with a side length of 71 μm. The CO_2 saturation $\mathrm{S}_{\mathrm{CO_2}}$ of each voxel was calculated as follows:

$$\mathrm{S}_{\mathrm{CO_2}} = c\left(\mathrm{CT}_{\mathrm{obs}} - \mathrm{CT}_{\mathrm{brine}}^{\mathrm{sat}}\right) = \frac{\mathrm{CT}_{\mathrm{obs}} - \mathrm{CT}_{\mathrm{brine}}^{\mathrm{sat}}}{\mathrm{CT}_{\mathrm{CO_2}}^{\mathrm{sat}} - \mathrm{CT}_{\mathrm{brine}}^{\mathrm{sat}}}, \quad (3)$$

where $\mathrm{CT}_{\mathrm{brine}}^{\mathrm{sat}}$ and $\mathrm{CT}_{\mathrm{CO_2}}^{\mathrm{sat}}$ are the voxel CT values of the brine-saturated and CO_2 saturated states, respectively, $\mathrm{CT}_{\mathrm{obs}}$ is the CT value of the considered saturation state, and the coefficient *c* relates $\mathrm{S}_{\mathrm{CO_2}}$ to the difference between the CT values.

Prior to experiment, the rock sample was vacuum-dried for two days. The dehydrated sample was pressurized by increasing the confining pressure from 0 to 15 MPa at 1-MPa intervals. Subsequently, the confining pressure was reduced to 5 MPa and the vacuumed sample was injected with brine (potassium iodide solution, 11.5 wt%) until fully saturated. The brine was continuously injected for measuring the permeability. Next, the poroelastic effect was investigated by elevating the confining and pore pressures to 15 MPa and 10 MPa, respectively, and the bulk modulus of the rock was calculated (Figure S7). Then CO_2 was injected into the coarse-grained end of the sample, initially at an injection of 10.1 MPa, with the sample outlet pressure maintained at 10 MPa. Under the low differential pressure, it took approximately 40 hours for the CO_2 fluid-flow front to reach the interface between the coarse- and fine-grained regions. The injection pressure was then increased to 10.3 MPa in 8 steps (approximately 1 hour/step), and eventually the CO_2 flow was able to overcome the capillary barrier and percolate into the low-permeability fine-grained region. The overall CO_2 injection lasted for approximately 68 hours. Finally, brine was injected into the sample under a higher pressure of ~10.8 MPa for about 20 hours. During these operations, the sample strain was continuously measured by the DFOSS system. In addition, the X-ray CT imaging was applied to monitor (during daytime hours) the spatial saturation of CO_2 in the rock sample.

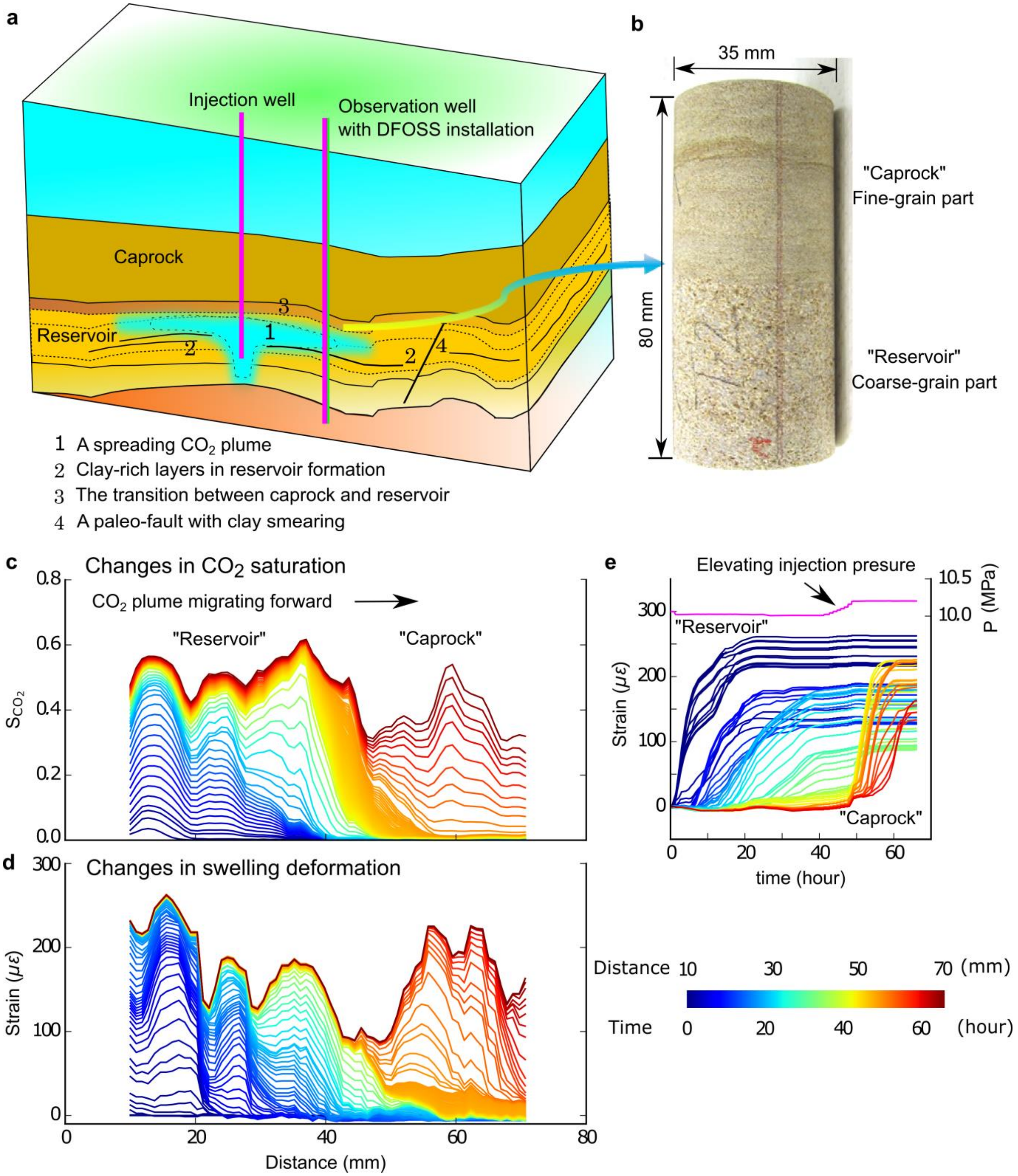

Figure 1. (**a**) Schematic model of a CO_2 storage site featuring an observation well with the DFOSS installation. Other features include the clay-rich components in the caprock–reservoir transition, the tight clay-rich layers in the reservoir formations, and paleo-faults with clay smearing. (**b**) The Tako sandstone sample used in this study may be considered as an analog of

reservoir–caprock systems or clay-rich layers. (**c**) Profiles of mean CO_2 saturation (SCO_2) (computed from X-ray CT imaging) along the rock sample. For clarity, the saturation data are linearly interpolated and colored by the elapsed time (see color bar). The raw data are shown in Figure S8. (**d**) Circumferential strain profiles (measured by DFOSS) on the surface of the rock sample. (**e**) Circumferential strain versus time curves, colored by spatial distance from the inlet end of the sample (see color bar). Note that as the pressure increased from 40 to 50 hours, the swelling-strain changes were marginal (< 10 με).

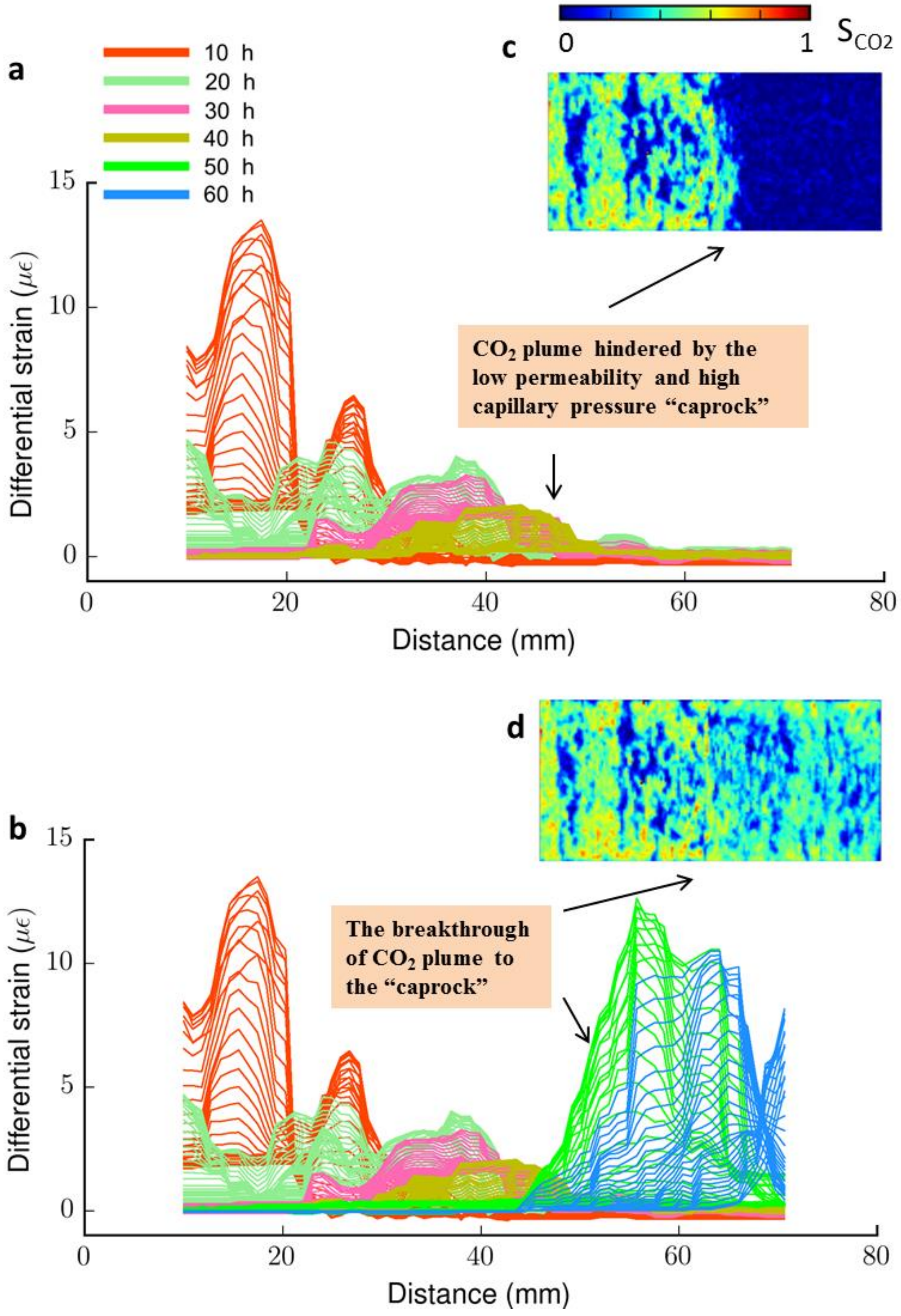

Figure 2. Differential strain changes calculated by subtracting two sets of measured strains with a time separation of approximately 3.3 hours. To emphasize the temporary changes, the overall

results are divided into six stages (each lasting for approximately 10 hours). (**a**) Changes before stage 5 (first 40 hours); (**b**) Changes in all stages. In (**a**) and (**b**), the colors indicate the different stages. Panels (**c**) and (**d**) are images of the CO_2 saturation (SCO_2) at 40 and 60 h, respectively. The structure-affected deformation behavior and the breakthrough of the CO_2 plume from the high permeability (reservoir) part to the low permeability (caprock) part are clearly observed.

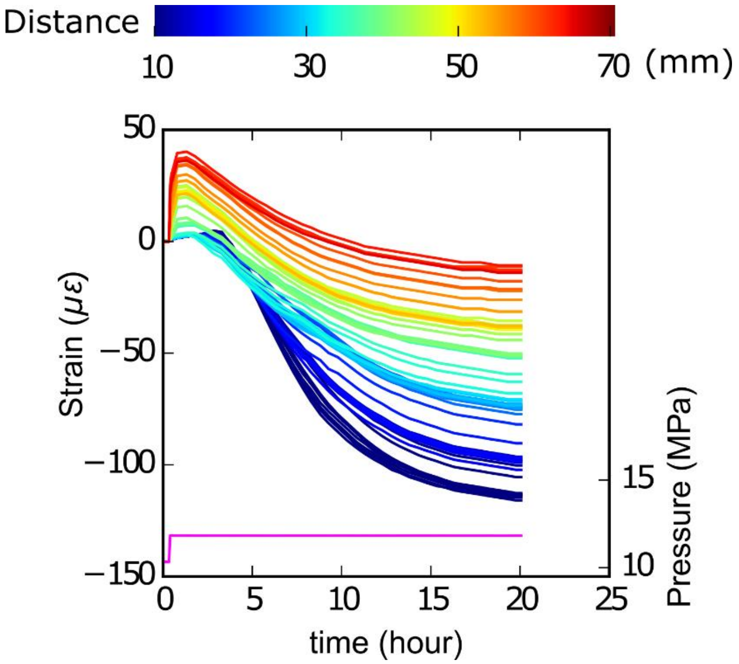

Figure 3. Strain changes (measured by DFOSS) during the brine re-imbibition after CO_2 drainage. Color bar denotes the spatial location along the sample.

3 Results: CO_2 plume migration and distributed strain responses

The DFOSS tool effectively monitored the deformations in the rock induced by CO_2/brine displacements. The strain changes well corresponded to the spreading of the CO_2 plume, and distinctly differed between the coarse- and fine-grained parts. As the CO_2 was injected, it displaced the brine from the rock sample, as indicated by the saturation changes calculated from the X-ray CT imaging (Figure 1c). As it migrated, the CO_2 plume was retarded by the low-permeability fine-grained part until the injection pressure was elevated. Before the breakthrough of the CO_2 plume to the fine-grain part, the corresponding strain (which gradually increased in magnitude from 0 to 260 μϵ) mainly responded in the coarse-grained region where the CO_2 plume developed (Figure 1d and e). Whereas the CO_2 gradients were steep near the CO_2 saturation front, the strain changes were gradual and occurred earlier than the CO_2 saturation changes, due to mechanical effects and the forward pressure migration.

The CO_2 plume broke into the fine-grained part after the injection pressure was step-elevated from 10.1 MPa to 10.3 MPa. The subsequent strain changes in the fine-grained part were large and rapid (Figure 1d and e). Under the experimental conditions, the breakthrough pressure of CO_2 percolating through the rock was below 300 kPa. The breakthrough behavior was well reflected in the strain signals, and the strain response to the pressure change (200 kPa) was well monitored. However, the pressure effect produced only a small strain (< 10 με) (Figure 1e). The large strain changes in the fine-grained part mainly followed the migration of the CO_2 plume with the CO_2/brine replacement. Generally, the changes accurately mirrored the migration of the CO_2/brine displacement front in the coarse-grained part and its breakthrough into the fine-grained part of the rock sample.

To better show the dynamic deformations and time-dependent behavior, we computed the differential strains between successive time steps (Figure 2a and b), which reflect the speed of the strain changes in different stages. In this calculation, the time interval between two sets of measured strains was approximately 3.3 hours. The overall results were divided into six stages (with a time interval of approximately 10 hours) to emphasize the temporary changes. Initially, the strain increase was rapid (Figure 2a and b). Once the CO_2 plume had migrated to a certain region (demarcated by the saturation images in Figure 2c and d), the strain changes became more gradual and eventually reached a near-stable state. Moreover, the strain changes spatially depended on the sedimentary structure. In several local low-porosity layers, the CO_2 saturation was lower than in other regions, and the strain changes were reduced in magnitude. These layers acted as temporal in-passing capillary barriers for the forward CO_2/brine displacement. In contrast to the CO_2 drainage, the rock sample during the brine imbibition swelled for a short period under the elevated pore pressure, and then showed a general shrinking trend (Figure 3). Like conventional strain gauges, the distributed strain changes obtained by the DFOSS technique revealed the mechanical deformation magnitude of the rock. However, they also provide rich information related to the fluid plume migration in the heterogeneous rock structure. Especially, analogously to a reservoir–caprock system, the CO_2 breakthrough from the coarse-grained part (reservoir) to the fine-grained part (caprock) was remarkably distinguished by the distributed strain signals.

4 Adsorption-induced swelling as an indicator of fluid displacement

Note that the strain changes in this study (~260 με) were much larger than would be expected under pure pore-pressure effects, as assumed in the poroelastic mechanism. In the fully brine-saturated state, the bulk modulus of the rock was approximately 7.6–8.8 GPa in the coarse-grained part and 8.3–10.0 GPa in the fine-grained part (see Figure S7). Consequently, under the given maximum change in effective pressure (300 kPa), the upper limit of the poroelastic (circumferential) deformation was expected to be smaller than 20 με. When the pore pressure increased during the drainage, the deformation limit well constrained the actual strain changes (< 10 με) induced by the pressure change alone (200 kPa) (Figure 1 e). In contrast, the measured strain values (~260 με) after displacing the brine with CO_2 far exceeded this limit. When the sample was fully saturated with brine, the strain even exceeded the strain generated by pore pressure changes of 200 MPa (approximately 100 με) (Figure S7b).

The large strain changes are likely related to the abundant content of clay mineral (kaolinite) in the rock. CO_2 is more readily adsorbed to clay minerals than brine. Several recent studies have shown that CO_2 can be adsorbed in clay-rich rocks, causing significant swelling (Busch et al., 2016). CO_2 adsorption in kaolinite is supported by both physicochemical studies (Chen & Lu, 2015; Heller & Zoback, 2014; Jedli et al., 2017) and direct experimental studies (Heller & Zoback, 2014). In kaolinite-bearing rock (i.e., shales), the swelling strain of CO_2 adsorption can be as large as ~10^3 με (Heller & Zoback, 2014). In clay materials, the adsorption ability of CO_2 is outstandingly higher than those of other fluids such as methane and water (Brochard et al., 2012).

When the brine was displaced by CO_2 during the drainage phase of the present experiment, the porous matrix of the clay-rich rock can cause a differential swelling of the porous matrix due to CO_2 adsorption as the CO_2 saturation increased (Figure 1). In contrast, during brine imbibition, the CO_2 desaturation and desorption by the replenished brine caused a shrinkage trend (Figure 3). The adsorption-induced swelling mechanism reasonably explains the magnitude of these changes (~260 $\mu\epsilon$).

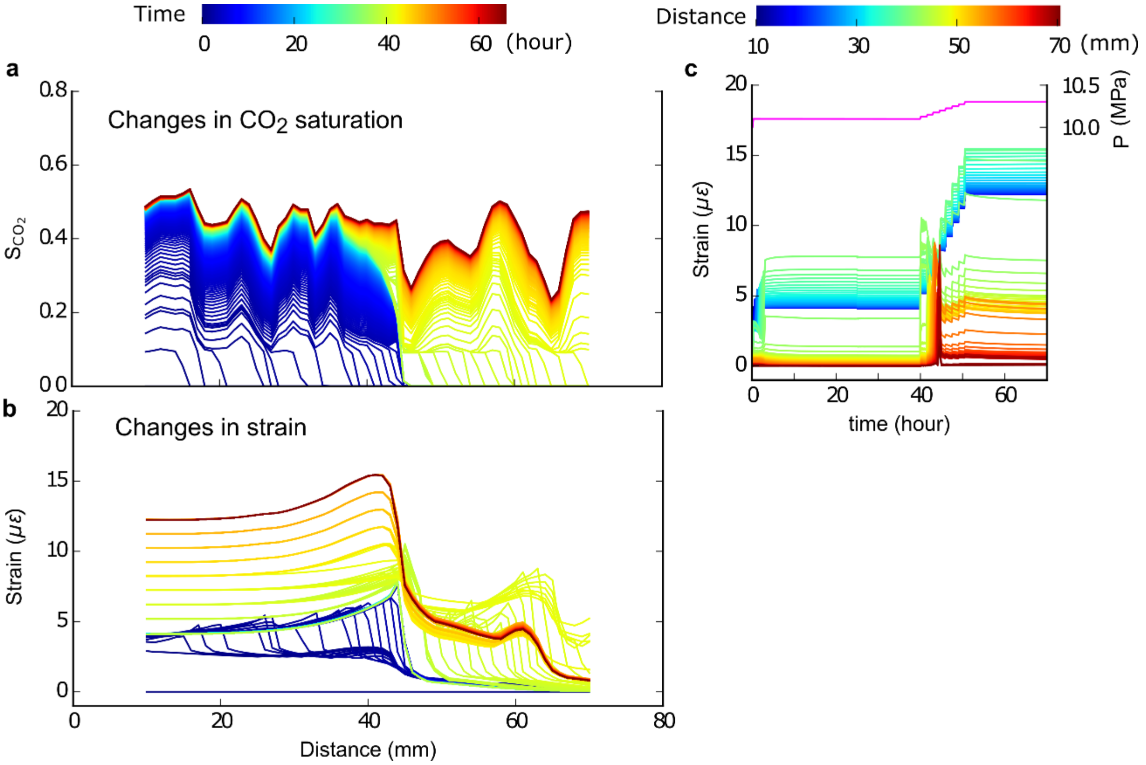

Figure 4. (**a**) Modeling results of averaged CO_2 saturation (SCO_2) along the rock sample. (**b**) Modeled profiles of circumferential strain caused by poroelastic deformation (without considering the adsorption-swelling effect). Colors in **a** and **b** denote time. (**c**) Modeled strain versus time plots. Colors in **c** denote the spatial distance to the inlet of the sample.

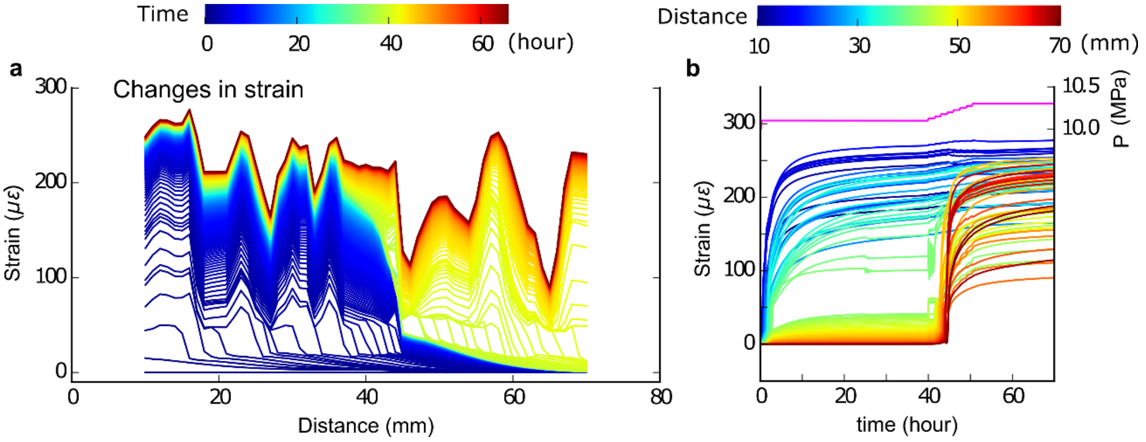

Figure 5. (**a**) Modeled profiles of circumferential strain, assuming that the sample is swollen by CO_2 adsorption on the clay mineral contents. (**b**) Modeled strain versus time plots. The saturation changes match those of Figure 4a.

We numerically simulated the effect of the adsorption-induced strain in a sequentially coupled one-dimensional two-phase fluid flow and poromechanical model (Appendix A). The adsorption-induced strain changes during CO_2 saturation were modeled by a Langmuir-type adsorption relationship with saturation scaling (Shi & Durucan, 2004). For comparison with the adsorption-included model, we estimated the maximum probable deformation due to the poroelastic mechanism alone, assuming the lower limit of the measured bulk modulus (7.6 GPa). The maximum circumferential strain was one order of magnitude smaller in the poroelastic model than in the adsorption-induced deformation mechanism (approximately 16 $\mu\epsilon$; see Figure 4, versus ~260 $\mu\epsilon$; see Figure 5). Note that the adsorption-inclusive model well interpreted the measured strains. Moreover, it generally reproduced the behavior of caprock breakthrough and the structure-dependent distributions of the saturation (Figure 4a) and deformations (Figure 5a). The rock porosity structure controls the spatial distribution of the capillary entry pressure, which further differentiates the spatial CO_2 saturation. Along with the pore pressure, the spatially distributed CO_2 saturation controls the adsorption-induced deformations. Such large-magnitude swellings were reported in several previous studies of CO_2 displacing brine in sandstone measured by conventional strain gauges (Xue & Ohsumi, 2004). However, the strains in these studies were not explicitly interpreted.

Clay-rich rocks are common in reservoir–caprock systems for geological storage of CO_2 and natural gas. These rocks may appear at the transition part between the reservoir and caprock, in the tight interbedding shale-contained layers in an overall high-permeability reservoir (Figure 1a), such as the CO_2 storage sites in Sleipner, Norway (Zweigel et al., 2004) and Nagaoka, Japan (Ito et al., 2017), and in sealed paleo-fault zones with clay smearing (Vrolijk et al., 2016). During the CO_2 injection and post-injection stages of large-scale CO_2 storage projects, the CO_2 migration and consequent deformation in these parts are critical, and must be closely monitored. Besides, even some of the reservoir formations targeted for CO_2 storage (e.g., the Tomakomai CO_2 storage site, Japan) are enriched in clay minerals (Okubo et al., 2011).

The strain changes in the clay-rich parts of our sample were much more sensitive to CO_2 adsorption than to pore pressure. As our core-scale study was a mini-proxy of an actual reservoir–caprock system, the changes in swelling strain might also indicate the migration of the CO_2 plume in field applications. That is, by monitoring the swelling strains, we could determine the passage of the CO_2 plume through the monitored regions (e.g., whether the plume has entered the clayey layers or lower portion of the caprock), and hence diagnose the potential risk of fluid leakage. The impact of the pore pressure build-up on deformation may increase with further CO_2 injection. From the deformation pattern and its magnitude, we can begin to distinguish between the effects of the pore pressure propagation (the pressure footprint) and the effects of CO_2 migration through the caprock (the saturation footprint (Juanes et al., 2010)). The former manifest as gradual changes from small to large deformations as the pressure increases; the latter induces a relatively large strain change within a short time once the CO_2 has migrated to the clay-rich part. When detecting CO_2 migrations around actual wellbores, the characteristics of natural clay-rich rocks could be actively supplemented by filler materials (such as bentonite or polymer) with a high adsorption-induced swelling property.

5 Conclusions

In a laboratory study, we straightforwardly demonstrated that the DFOSS technique accurately measures the distributed strain signals in rocks during supercritical CO_2/brine displacement, under the typical conditions of CO_2 geological storage. Simultaneously, we observed the fluid distributions, thereby verifying the migration and breakthrough behavior of the CO_2 plume. The enhanced swelling-strain signals caused by CO_2 adsorption on/in the clay minerals can detect CO_2 appearances in the clay-rich critical parts in a reservoir–caprock system (the transition part between a caprock and a reservoir, the clay-rich interbedding layers in the reservoir, and the clay-smearing fault zones). Therefore, they provide a practical indicator for monitoring CO_2 flow behavior in the field. Here we focused on the strain responses to CO_2 injections, which are relevant to CO_2 storage in underground reservoirs. However, the idea of fluid-tracking by induced deformation is not limited to CO_2. Any geo-fluid activities that induce rock deformations, such as pore pressure build-up, adsorption, osmosis, and other fluid–fluid or fluid–solid reactions, could be tracked in this way. The DFOSS technique improves our understanding of fluid behavior and rock deformation in underground reservoirs, and should be helpful in verifying the secure containment of reservoir–caprock systems.

In field-scale applications, DFOSS can only be installed in an underground reservoir along a drilled wellbore, where it would measure the strain behind the wellbore casing (Xue & Hashimoto, 2017). CO_2 plume migration can be directly monitored when the plume reaches the wellbore vicinity and spreads vertically, or can be inferred from the induced mechanical deformations propagated from far regions. In any case, a geomechanical simulation would reveal the relationship between the evolving strain magnitude and fluid activity. In practice, the distributed strain measurements can be integratively analyzed with information obtained from other methods, such as pressure (Strandli & Benson, 2013) and temperature (Zhang et al., 2018) monitoring, electrical measurements (Bergmann et al., 2017), seismic (Arts et al., 2004) and microseismic monitoring (Verdon et al., 2013). Especially, DFOSS can be employed together with the distributed acoustic sensing (Daley et al., 2015). An integrated methodology would more solidly track the CO_2 plume and diagnose potential geomechanical and fluid flow problems in the reservoir–caprock system. One potential problem in this study is the possible swelling effect of the epoxy adhesives when contacted with CO_2. If used as the firming materials of the DFOSS fibers, these epoxies would affect the measured rock deformation. This effect should be investigated in future work.

Appendix A

A1 Adsorption-induced swelling strain model

The adsorption induced swelling strain ε in confined pores can be described by a refined poromechanical model (Vermorel & Pijaudier-Cabot, 2014)

$$\varepsilon = \varepsilon_0 + \int_{P_{b0}}^{P_b} \frac{\mathrm{d}P_b}{M}\{\alpha(1-\chi)^{-1}-1\}, (1)$$

where ε_0 is the initial strain, M is the bulk modulus, α is the Biot's coefficient, P_0 and P_b

$$\mathrm{d}P_f = \frac{\mathrm{d}P_b}{1-\chi} (2)$$

The swelling strain predicted by Equation (1) is similar to that in the Langmuir-type sorption model. Analytically, it is equivalent to an empirical Langmuir-type deformation model (Levine, 1996; Shi & Durucan, 2004),

$$\varepsilon_{\mathrm{sorp}} = \frac{\varepsilon_{\mathrm{max}} P}{P + P_{\varepsilon}} \; (3)$$

where $\varepsilon_{\mathrm{sorp}}$ is the adsorption-induced volumetric strain at pressure P, and $\varepsilon_{\mathrm{max}}$ and P_{ε} are similar to the strain-scaling constants in the Langmuir-type model.

Numerical simulations were performed on a sequentially coupled one-dimensional two-phase fluid flow and poromechanical model, which is based on an open source reservoir simulator (Lie, 2014).

The two-phase fluid flow equation is given by

$$\frac{\phi \rho_{\alpha} S_{\alpha}}{\partial t} + \nabla \cdot (\rho_{\alpha} v_{\alpha}) = \rho_{\alpha} Q_{\alpha}, \; (4)$$

where ϕ is the porosity, α denotes the fluid type (wetting (w) or nonwetting (nw)), ρ and S are the density and saturation of the fluids, respectively, and Q is the source. The flow flux v is expressed by the extended Darcy's law

$$v_{\alpha} = -\frac{K k_{\mathrm{r}\alpha}}{\mu_{\alpha}} (\nabla p_{\alpha} - \rho_{\alpha} g \nabla h), \; (5)$$

where K and $k_{\mathrm{r}\alpha}$ are the absolute and relative permeabilities, respectively, μ_{α} is the fluid viscosity, p is the pressure, and $\rho_{\alpha} g \nabla h$ accounts for the gravity force.

In the modeling process, the permeability at each location was estimated by the following Leverett J-function (Krause et al., 2013):

$$\mathrm{K_i} = \phi_{\mathrm{i}} \frac{1}{\overline{\mathrm{P_c}}(\mathrm{S_w})^2} [\sigma \cos(\theta) \mathrm{J}(\mathrm{S_{w,i}})]^2, \; (6)$$

where *i* denotes the spatial location, σ and θ are the interfacial tension and contact angle between the CO_2 and brine, respectively, and $\overline{P_{\mathrm{c}}}$ is the global capillary pressure at each saturation (S_{w}) estimated by the mercury injection method. The Leverett J-function J is expressed as

$$J(S_{\mathrm{w}}) = \frac{P_{\mathrm{c}}}{\sigma \cos\theta} \sqrt{\frac{k}{\phi}}. \; (7)$$

To account for the local capillary pressure, the global capillary pressure is scaled by the local porosity ratio as follows:

$$P_{\mathrm{c}}(S_{\mathrm{w}}, i) = \overline{P_{\mathrm{c}}}(S_{\mathrm{w}}, i) \left(\frac{\phi_0}{\phi}\right)^n, \; (8)$$

where ϕ_0 is the mean porosity and n is a tuning exponent.

The mechanical responses are modeled by the following equations:

$$\nabla \cdot \sigma_{ij} + f = 0, \; (9)$$

$$\varepsilon_{ij} = \frac{1}{2}\left(\nabla u_i + \nabla u_j\right), \; (10)$$

$$\varepsilon_{\mathrm{ij}} = \frac{1}{2G} \sigma_{ij} - \left(\frac{1}{6G} - \frac{1}{9K}\right) \sigma_{kk} \delta_{ij} + \frac{b}{3K} p \delta_{ij} + \frac{\varepsilon_{sorp}}{3} \delta_{ij}. \; (11)$$

where σ_{ij} and ε_{ij} are elements of the stress and strain tensors, respectively, f is the body force, u_i is the displacement, and G and K are the shear and bulk moduli, respectively. b is the Biot's coefficient, p is the pore pressure, δ_{ij} is the Kronecker delta, and ε_{sorp} is the adsorption-induced strain.

References

Arts, R., Eiken, O., Chadwick, A., Zweigel, P., Van der Meer, L., & Zinszner, B. (2004). Monitoring of CO2 injected at Sleipner using time-lapse seismic data. *Energy*, *29*(9–10), 1383–1392.

Benson, S., Cook, P., Anderson, J., Bachu, S., Nimir, H. B., Basu, B., et al. (2005). Underground geological storage. *IPCC Special Report on Carbon Dioxide Capture and Storage*, 195–276.

Bergmann, P., Schmidt ‐ Hattenberger, C., Labitzke, T., Wagner, F. M., Just, A., Flechsig, C., & Rippe, D. (2017). Fluid injection monitoring using electrical resistivity tomography—five years of CO2 injection at Ketzin, Germany. *Geophysical Prospecting*, *65*(3), 859–875.

Brochard, L., Vandamme, M., Pellenq, R. J.-M., & Fen-Chong, T. (2012). Adsorption-induced deformation of microporous materials: coal swelling induced by CO2–CH4 competitive adsorption. *Langmuir*, *28*(5), 2659–2670.

Busch, A., Bertier, P., Gensterblum, Y., Rother, G., Spiers, C. J., Zhang, M., & Wentinck, H. M. (2016). On sorption and swelling of CO2 in clays. *Geomechanics and Geophysics for Geo-Energy and Geo-Resources*, *2*(2), 111–130.

Cameron, D. A., Durlofsky, L. J., & Benson, S. M. (2016). Use of above-zone pressure data to locate and quantify leaks during carbon storage operations. *International Journal of Greenhouse Gas Control*, *52*, 32–43. https://doi.org/https://doi.org/10.1016/j.ijggc.2016.06.014

Celia, M. A. (2017). Geological storage of captured carbon dioxide as a large-scale carbon mitigation option. *Water Resources Research*. https://doi.org/10.1002/2017WR020841

Chen, Y.-H., & Lu, D.-L. (2015). CO2 capture by kaolinite and its adsorption mechanism. *Applied Clay Science*, *104*, 221–228.

Daley, T. M., Miller, D. E., Dodds, K., Cook, P., & Freifeld, B. M. (2015). Field testing of modular borehole monitoring with simultaneous distributed acoustic sensing and geophone vertical seismic profiles at Citronelle, Alabama. *Geophysical Prospecting*, n/a-n/a. https://doi.org/10.1111/1365-2478.12324

Gan, W., & Frohlich, C. (2013). Gas injection may have triggered earthquakes in the Cogdell oil field, Texas. *Proceedings of the National Academy of Sciences*, *110*(47), 18786–18791.

Heller, R., & Zoback, M. (2014). Adsorption of methane and carbon dioxide on gas shale and pure mineral samples. *Journal of Unconventional Oil and Gas Resources, 8,* 14–24.

Hincks, T., Aspinall, W., Cooke, R., & Gernon, T. (2018). Oklahoma's induced seismicity strongly linked to wastewater injection depth. *Science*, *7911*(February), 1–9. https://doi.org/10.1126/science.aap7911

Ito, T., Ohbuchi, A., Nakajima, T., & Xue, Z. (2017). Identifying the source of natural gamma-rays in shallow-marine siliciclastic strata and their significance for shale evaluation: A case study of the CO2 storage aquifer at the Nagaoka site, Japan. *Journal of Natural Gas Science and Engineering*, *46*, 782–792.

Jedli, H., Jbara, A., Hedfi, H., Bouzgarrou, S., & Slimi, K. (2017). Carbon dioxide adsorption isotherm study on various cap rocks in a batch reactor for CO2 sequestration processes. *Applied Clay Science*, *136*, 199–207. https://doi.org/10.1016/j.clay.2016.11.022

Juanes, R., MacMinn, C. W., & Szulczewski, M. L. (2010). The footprint of the CO 2 plume during carbon dioxide storage in saline aquifers: storage efficiency for capillary trapping at the basin scale. *Transport in Porous Media*, *82*(1), 19–30.

Kishida, K., Yamauchi, Y., & Guzik, A. (2014). Study of optical fibers strain-temperature sensitivities using hybrid Brillouin-Rayleigh System. *Photonic Sensors*, *4*(1), 1–11.

Kogure, T., & Okuda, Y. (2018). Monitoring the Vertical Distribution of Rainfall ‐ Induced Strain Changes in a Landslide Measured by Distributed Fiber Optic Sensing With Rayleigh Backscattering. *Geophysical Research Letters*, *0*(0). https://doi.org/10.1029/2018GL077607

Kogure, T., Horiuchi, Y., Kiyama, T., Nishizawa, O., Xue, Z., & Matsuoka, T. (2015). Fiber optic strain measurements using distributed sensor system under static pressure conditions. *BUTSURI-TANSA(Geophysical Exploration)*, *68*(1), 23–38. https://doi.org/10.3124/segj.68.23

Koyamada, Y., Imahama, M., Kubota, K., & Hogari, K. (2009). Fiber-optic distributed strain and temperature sensing with very high measurand resolution over long range using coherent OTDR. *Journal of Lightwave Technology*, *27*(9), 1142–1146.

Krause, M., Krevor, S., & Benson, S. M. (2013). A procedure for the accurate determination of sub-core scale permeability distributions with error quantification. *Transport in Porous Media*, *98*(3), 565–588.

Levine, J. R. (1996). Model study of the influence of matrix shrinkage on absolute permeability of coal bed reservoirs. *Geological Society, London, Special Publications*, *109*(1), 197–212. https://doi.org/10.1144/GSL.SP.1996.109.01.14

Li, Y. (2016). Development and evaluation of a coaxial cable sensing system for CO 2 sequestration wellbore integrity monitoring.

Lie, K.-A. (2014). An introduction to reservoir simulation using MATLAB: user guide for the Matlab Reservoir Simulation Toolbox (MRST). SINTEF ICT.

Maharramov, M., & Zoback, M. D. (2018). Monitoring of cyclic steam stimulation by inversion of surface tilt measurements. *The Leading Edge*, *37*(5), 350–355.

Okubo, S., Takahashi, K., & Nakashima, H. (2011). The relationship between the expandability of clay mineral and the permeability of Takinoue pyroclastic layer “T1 member” in Yufutsu Oil and Gas Field, Hokkaido, Japan. *Journal of the Japanese Association for Petroleum Technology*, *76*(3), 209–218. https://doi.org/10.3720/japt.76.209

Rambow, F., Dria, D., Childers, B., Appel, M., Freeman, J., Shuck, M., et al. (2010). Real-Time Fiber-Optic Casing Imager. *SPE Journal*, *15*(4), 1095–1103. https://doi.org/10.2118/109941-PA

Romanov, V., & Myshakin, E. M. (2018). Experimental Studies: Clay Swelling. In *Greenhouse Gases and Clay Minerals* (pp. 125–145). Springer.

Rutqvist, J. (2012). The geomechanics of CO 2 storage in deep sedimentary formations. *Geotechnical and Geological Engineering*, *30*(3), 525–551. https://doi.org/10.1007/s10706-011-9491-0

Rutqvist, J., & Tsang, C.-F. (2002). A study of caprock hydromechanical changes associated with CO2-injection into a brine formation. *Environmental Geology*, *42*(2), 296–305. https://doi.org/10.1007/s00254-001-0499-2

Sanchez, D. L., Johnson, N., McCoy, S. T., Turner, P. A., & Mach, K. J. (2018). Near-term deployment of carbon capture and sequestration from biorefineries in the United States. *Proceedings of the National Academy of Sciences*, *115*(19), 4875–4880.

Shi, J., & Durucan, S. (2004). Drawdown induced changes in permeability of coalbeds: a new interpretation of the reservoir response to primary recovery. *Transport in Porous Media*, *56*(1), 1–16.

Shi, J., Sinayuc, C., Durucan, S., & Korre, A. (2012). Assessment of carbon dioxide plume behaviour within the storage reservoir and the lower caprock around the KB-502 injection well at In Salah. *International Journal of Greenhouse Gas Control*, *7*, 115–126.

Shirzaei, M., Ellsworth, W. L., Tiampo, K. F., González, P. J., & Manga, M. (2016). Surface uplift and time-dependent seismic hazard due to fluid injection in eastern Texas. *Science*, *353*(6306), 1416–1419.

Strandli, C. W., & Benson, S. M. (2013). Identifying diagnostics for reservoir structure and CO2 plume migration from multilevel pressure measurements. *Water Resources Research*, *49*(6), 3462–3475.

Sun, Y., Li, Q., & Fan, C. (2017). Laboratory core flooding experiments in reservoir sandstone under different sequestration pressures using multichannel fiber Bragg grating sensor arrays. *International Journal of Greenhouse Gas Control*, *60*, 186–198. https://doi.org/10.1016/j.ijggc.2017.03.015

Vasco, D. W., Rucci, A., Ferretti, A., Novali, F., Bissell, R. C., Ringrose, P. S., et al. (2010). Satellite‐based measurements of surface deformation reveal fluid flow associated with the geological storage of carbon dioxide. *Geophysical Research Letters*, *37*(3).

Verdon, J. P., Kendall, J.-M., Stork, A. L., Chadwick, R. A., White, D. J., & Bissell, R. C. (2013). Comparison of geomechanical deformation induced by megatonne-scale CO2 storage at Sleipner, Weyburn, and In Salah. *Proceedings of the National Academy of Sciences of the United States of America*, *110*(30), E2762-71. https://doi.org/10.1073/pnas.1302156110

Vermorel, R., & Pijaudier-Cabot, G. (2014). Enhanced continuum poromechanics to account for adsorption induced swelling of saturated isotropic microporous materials. *European Journal of Mechanics, A/Solids*, *44*, 148–156. https://doi.org/10.1016/j.euromechsol.2013.10.010

Vrolijk, P. J., Urai, J. L., & Kettermann, M. (2016). Clay smear: Review of mechanisms and applications. *Journal of Structural Geology*, *86*, 95–152.

Wan, J., Tokunaga, T. K., Ashby, P. D., Kim, Y., Voltolini, M., Gilbert, B., & DePaolo, D. J. (2018). Supercritical CO2 uptake by nonswelling phyllosilicates. *Proceedings of the*

National Academy of Sciences. Retrieved from http://www.pnas.org/content/early/2018/01/09/1710853114.abstract

Wentinck, H. M., & Busch, A. (2017). Modelling of CO2 diffusion and related poro-elastic effects in a smectite-rich cap rock above a reservoir used for CO2 storage. *Geological Society, London, Special Publications*, *454*(1), 155–173.

White, J. A., Chiaramonte, L., Ezzedine, S., Foxall, W., Hao, Y., Ramirez, A., & McNab, W. (2014). Geomechanical behavior of the reservoir and caprock system at the In Salah CO2 storage project. *Proceedings of the National Academy of Sciences*, *111*(24), 8747–8752.

Wu, Q., Nair, S., Shuck, M., van Oort, E., Guzik, A., & Kishida, K. (2017). Advanced distributed fiber optic sensors for monitoring real-time cementing operations and long term zonal isolation. *Journal of Petroleum Science and Engineering*, *158*(August), 479–493. https://doi.org/10.1016/j.petrol.2017.08.072

Xue, Z., & Hashimoto, T. (2017). Geomechanical Monitoring of Caprock and Wellbore Integrity Using Fiber Optic Cable: Strain Measurement from the Fluid Injection and Extraction Field Tests. *Energy Procedia*, *114*(Supplement C), 3305–3311. https://doi.org/https://doi.org/10.1016/j.egypro.2017.03.1462

Xue, Z., & Ohsumi, T. (2004). Seismic wave monitoring of CO2 migration in water-saturated porous sandstone. *Exploration Geophysics*, *35*(1), 25–32.

Xue, Z., Park, H., Kiyama, T., Hashimoto, T., Nishizawa, O., & Kogure, T. (2014). Effects of hydrostatic pressure on strain measurement with distributed optical fiber sensing system. *Energy Procedia*, *63*, 4003–4009. https://doi.org/https://doi.org/10.1016/j.egypro.2014.11.430

Zhang, Y., Jung, Y., Freifeld, B., & Finsterle, S. (2018). Using distributed temperature sensing to detect CO 2 leakage along the injection well casing. *International Journal of Greenhouse Gas Control*, *74*, 9–18.

Zoback, M. D., & Gorelick, S. M. (2012). Earthquake triggering and large-scale geologic storage of carbon dioxide. *Proceedings of the National Academy of Sciences of the United States of America*, *109*(26), 10164–8. https://doi.org/10.1073/pnas.1202473109

Zweigel, P., Arts, R., Lothe, A. E., & Lindeberg, E. B. G. (2004). Reservoir geology of the Utsira Formation at the first industrial-scale underground CO2 storage site (Sleipner area, North Sea). *Geological Society, London, Special Publications*, *233*(1), 165–180.

Acknowledgments

This paper is based on results obtained from a project commissioned by the New Energy and Industrial Technology Development Organization (NEDO) and the Ministry of Economy, Trade and Industry (METI) of Japan. Data to support this research are available from the following link: https://dx.doi.org/10.17605/OSF.IO/R6W8F. Y.Z. thanks Y. Yamauchi, M. Yokoyama and Y. Okabayashi in Neubrex Co., Ltd for their technical support and Y. Sun for his help in comment the manuscript. We are thankful to anonymous reviewers and associated editor Tetsu Tokunaga who helped comment the manuscript.

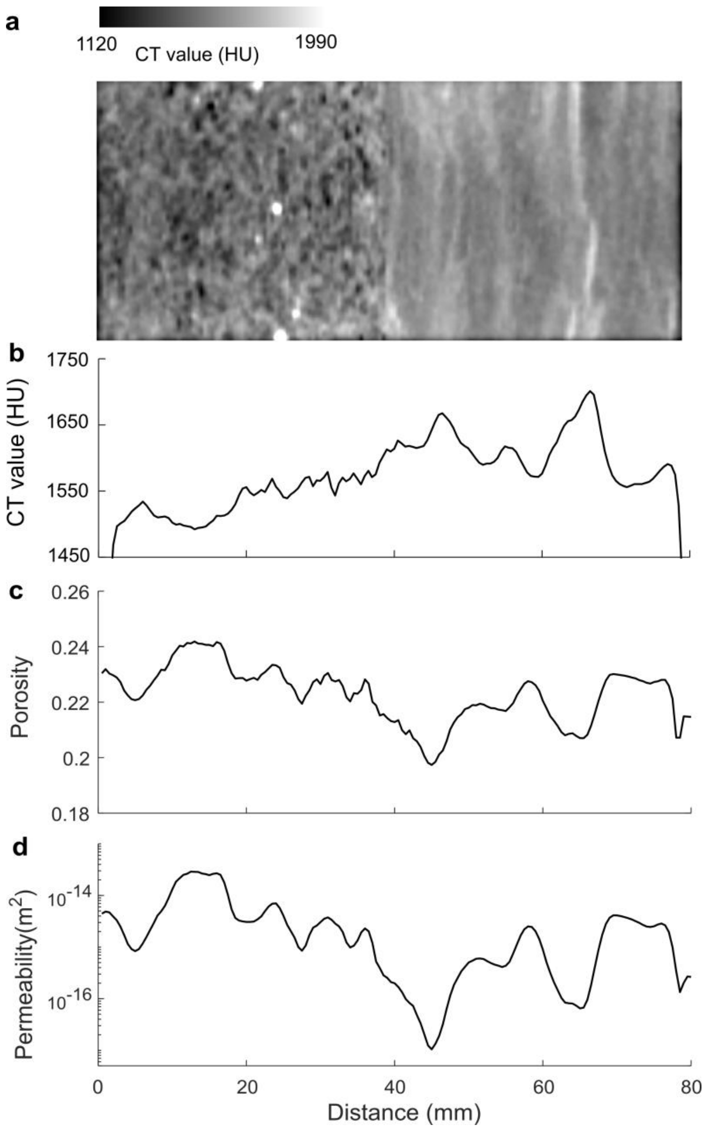

Figure S1. (**a)** Sectional X-ray CT image of dried rock showing its contrasting inner structure. The image intensity is expressed by the Hounsfield CT value, which is basically proportional to the void density. (**b**) Profile of average CT values along the sample axis. (**c**) Porosity profile calculated from X-ray CT images obtained in the dry and brine-saturated states. (**d**) Permeability profile estimated by the Leverett J-function (see Appendix A).

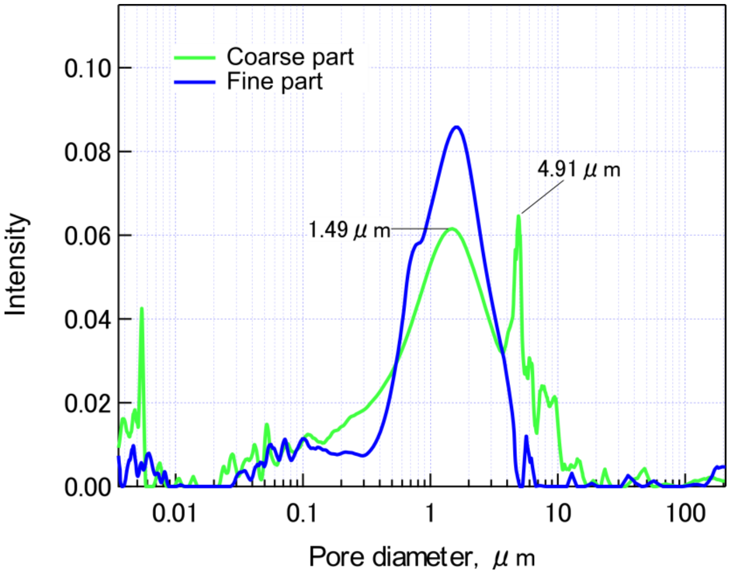

Figure S2. Pore-size distributions of the coarse-grained and fine-grained parts of the rock sample (Tako sandstone) measured by the mercury injection method.

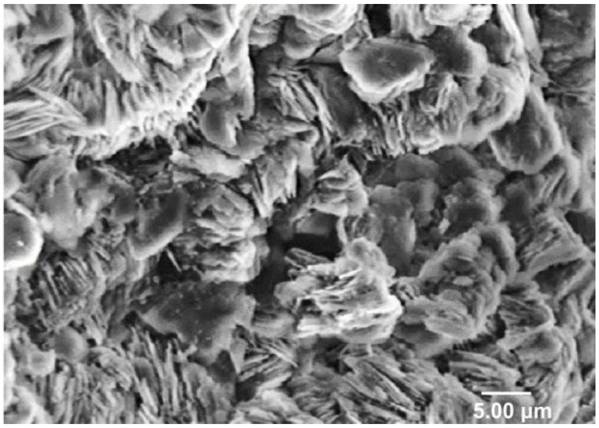

Figure S3. Scanning electron microscope (SEM) photo showing kaolinite platelets in the Tako sandstone sample.

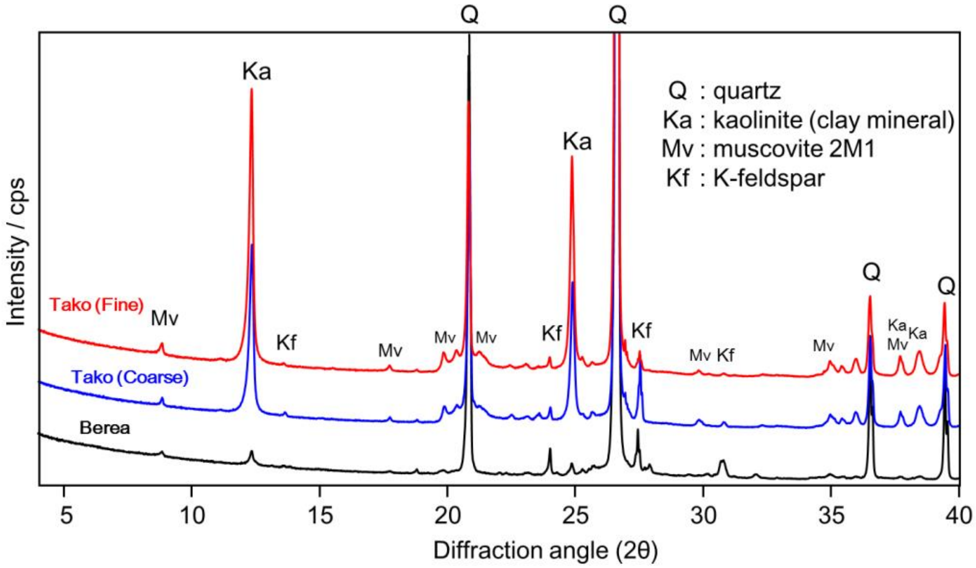

Figure S4. X-ray powder diffraction (XRD) spectra of the fine-grained and coarse-grained parts of the Tako sandstone. The spectrum of the well-known Berea sandstone is plotted for comparison.

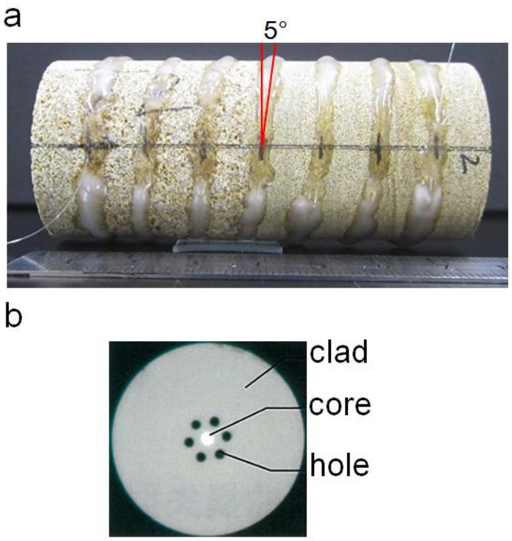

Figure S5. (a) Photograph of the rock sample (Tako sandstone) with the single-mode holey optical fiber fabricated from silica and spirally bonded to the sample surface. The fiber was firmly adhered to the sample by epoxy adhesive. (b) Axial photograph showing the structure of the holey optical fiber.

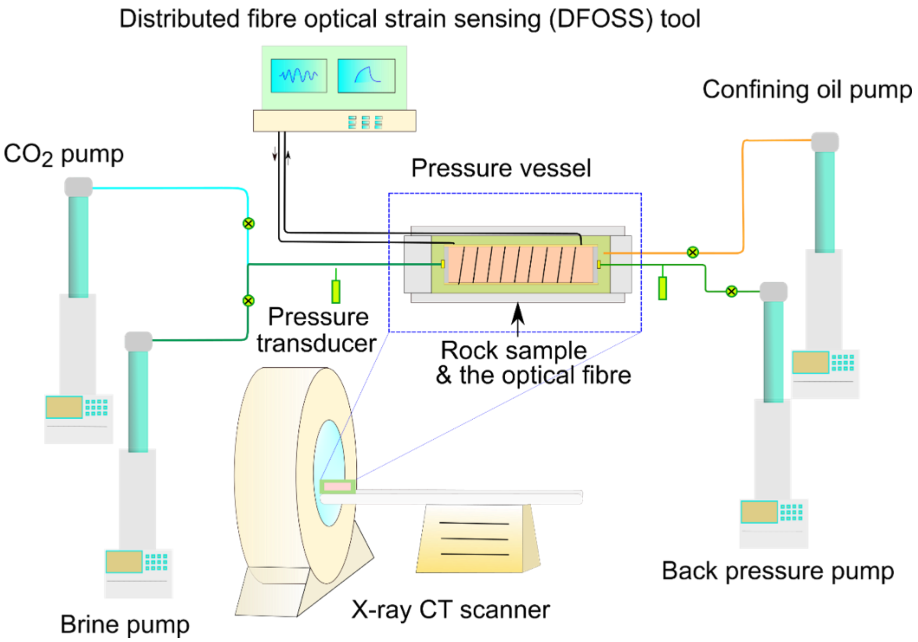

Figure S6. Schematic of the measurement system. The main components are a medical X-ray CT scanner, a pressure vessel, a distributed fiber-optical strain sensing (DFOSS) tool, several syringing pumps, and two pressure transducers.

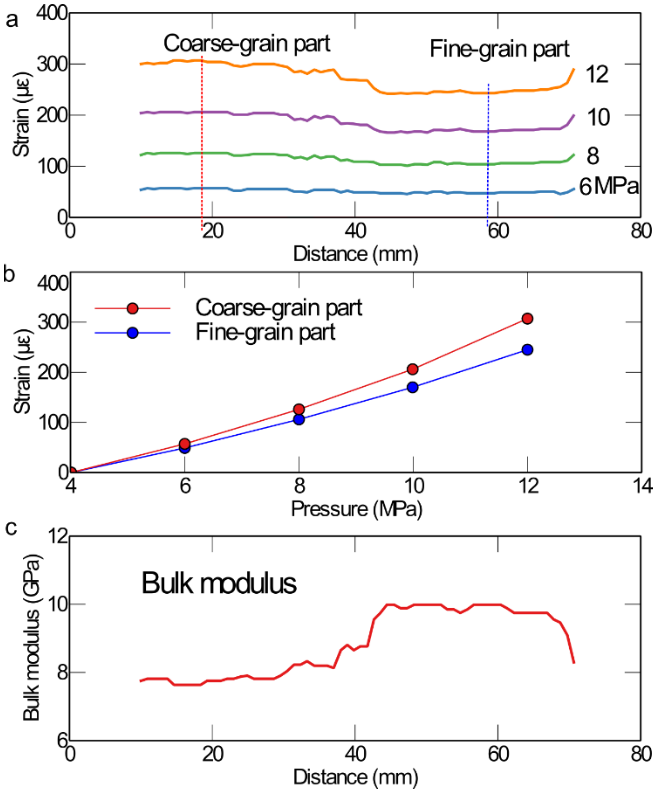

Figure S7. Strain changes as the pore pressure increases from 4 to 12 MPa under a constant confining pressure (15 MPa). (**a**) Strain profiles along the sample axis. (**b**) Strain versus pore pressure at two selected spatial points (see a for locations), one in the coarse-grained part, the other in the fine-grained part. **c**, Bulk modulus profile determined from the measured distributed strain data near the pressure condition (10 MPa) of CO_2 drainage. The spatial average, minimum, and maximum values of the bulk modulus are 8.8 GPa, 7.6 GPa and 10.0 GPa, respectively.

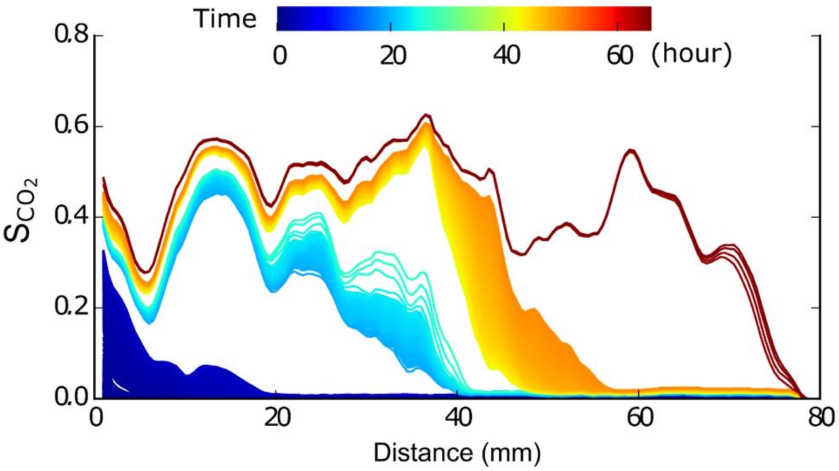

Figure S8. Measured spatially averaged CO_2 saturations (S_{CO2}) along the sample axis. Color denotes time since CO_2 injection (drainage). Data blanks are sourced from unviable measurements outside the worktime.